Localized folding of thick layers

Pouria Behnoudfar [a,*], Bruce E. Hobbs [a,b], Alison Ord [b], Luis Espath [c], Victor M. Calo [d]

[a] Mineral Resources, Commonwealth Scientific and Industrial Research Organisation (CSIRO), Kensington, Perth, WA, 6152, Australia
[b] School of Earth and Environment, The University of Western Australia, Crawley, WA, 6009, Australia
[c] School of Mathematical Sciences, University of Nottingham, Nottingham, NG7 2RD, United Kingdom
[d] School of Electrical Engineering, Computing and Mathematical Sciences, Curtin University, P.O. Box U1987, Perth, WA, 6845, Australia

ARTICLE INFO

ABSTRACT

We describe the localized folding of thick layers embedded in a viscoelastic framework. Higher-order partial differential equations such as the Swift-Hohenberg equation are standard for modelling the folding process. Using a high-order shear theory, we modify the Swift-Hohenberg equation to describe the buckling of thick layers and consider the folded layer's viscoelastic behavior. The use of thick layers enables us to consider shear strains parallel to the layers during folding. Our model naturally captures the softening-stiffening behavior by including a non-linear viscoelastic description using a Winkler-type foundation. Next, we study the linear stability behavior of the system and derive the dispersion relations. Finally, we simulate this new model using a robust custom-built isogeometric analysis solver, which allows us to describe thick folded layers with localized folding. The numerical results show that the folding of an elastic layer produces periodic patterns while a viscoelastic layer deflects locally. When the horizontal forces are unequal, the periodic folds initiate in the direction of the smaller force and the localized deformations occur parallel to the larger force. Later, the nonlocal deformation occurs in the direction of a smaller force. Domes and basins or more linear ridges and valleys are formed according to the relative magnitudes of the applied forces. Domes and basins are the results of equal horizontal applied forces, and non-equal forces result in ridges and valleys.

1. Introduction

John Ramsay was one of the great observers of Structural Geology, firmly rooted in observing structures in the field where interpretations were made in terms of the strain fields that conceivably exist in deformed rocks. In some ways, he was perhaps lucky to have undertaken a lot of his work before the theoretical studies of Biot became entrenched as a dogma in the study of folds since his observations, unlike those of a host of others, were not clouded by the interpretations and generalizations associated with Biot's results. Although Ramsay (1967) acknowledges Biot's work as "stimulating", except for quoting and accepting Biot's scaling effect of wavelength in terms of layer thickness, he shows and discusses a range of fold geometries and processes based on field observations and unrelated to Biot's arguments. In particular, these examples involve localized folding, and various processes that lead to non-concentric folding; The experimental folds of John Ramsay [27, Figures 3.51, 7.29, 7.35] and others (Blay et al., 1977; Cobbold, 1976; Hudleston, 1973; Watkinson, 1976) are localized rather than strictly periodic. The 3D model introduced in (M ü hlhaus et al., 1998) describes basins and valleys as localized folded structures. Biot's folding theory assumes that the buckling layer is thin compared to its deflection; thus, we assume $\sin(\theta) = \theta$ with θ being the deflection angle, which, when used in Biot's buckling equation, we describe as a linear combination of sines and cosines with a resultant range of wavelengths. Biot proceeded to show that just one wavelength grows fastest so that the resulting profile is always periodic. Many attempted extensions of the thin layer, small deflection theory to thick layers had little success (Fletcher, 1974; Schmalholz and Podladchikov, 2000; Smith, 1975, 1977). The issue is that the buckling of thick layers involves shear strains parallel to the layer, whereas such strains are small and neglected in thin layers. Thus, nonlinearity appears when studying the finite buckling of thick layers both by the complexity of the strain field and the displacement field description. This paper addresses both issues.

Spatially localized structures and deformations are studied in various fields such as reaction-diffusion systems (Lee et al., 1994), liquid crystals (Joets and Ribotta, 1988; Kolodner, 1993; Lakes and Lakes, 2009; Lee et al., 1994; Love, 2013; M ü hlhaus et al., 1998; Piegl and Tiller, 1987; Pirkl et al., 1993), and binary fluid flows (Kolodner, 1993).

* Corresponding author.
 E-mail addresses: pouria.behnoudfar@csiro.au, p.behnoud@gmail.com (P. Behnoudfar).

Table 1

Symbols used in this paper, units and typical values.

Quantity	Description	Units, typical values
E	Young's modulus for layer	$4.5 \times 10^9 \ Pa$
h	Thickness of layer	m
t	time	s
$\mathbf{u}$	Displacement field	(m, m, m)
ε_{ij}	Strain tensor	Dimensionless
η	Viscosity of embedding layer	$Pa \ s$
δw	deflection Perturbation	m
$\mathbf{k}$	vector of modes	Dimensionless
τ_c	Viscosity of layer	$Pa \ s$
c	factor: $\dfrac{4}{3h^2}$	m^{-2}
λ	Nondimensional viscosity	Dimensionless
$\widehat{\lambda}$	Nondimensional viscosity of Maxwell material	Dimensionless
P	axial force	N
ν	Poisson's ratio	0.3 Dimensionless
k_1, k_2, k_3	Stiffness of the framework	N/m
μ	viscoelastic response	N/m
κ	Curvature	m^{-1}
γ_{ij}	Transverse strain	Dimensionless
Ω	3D domain	Geometry
Ω_0	2D middle surface	Geometry
σ	dispersion relation	Dimensionless
ζ	Rotation of the normal vector	Degrees
D	Bending stiffness	$Pa \ m^3$
w	Vertical deflection	m
w_b	Vertical deflection due to bending	m
w_s	Vertical deflection due to transverse shear strains	m
Δ	Laplacian	Operator
subscript e	Elastic contribution	–
subscript v	Viscous contribution	–
x	Spatial coordinate	Dimensionless
L	Plate's horizontal dimension	m
$f_e(u)$	Resistive elastic force applied by framework	N
$f_v(u)$	Resistive viscous force applied by framework	N
$\Pi(w)$	Energy functional of the system	function
$\Psi(w)$	Evolution functional of the system	function

Table 2

Applied mathematical procedures in this paper.

Term	Description
Isogeometric analysis (IGA) discretization	A finite element method using NURBS as basis functions and delivers elements with higher global continuity [8, 9].
Non-uniform rational B-spline (NURBS)	Mathematical model using basis splines (B-splines) for representing curves and surfaces (Piegl and Tiller, 1987).
Galerkin method	It converts a continuous weak formulation problem to a discrete problem by applying linear constraints determined by finite sets of basis functions (Hughes, 2012).
Newton's method	An iterative algorithm for finding the roots of a differentiable function (Atkinson, 2008).
Dirichlet boundary condition	It specifies the values that a solution needs to take along the boundary of the domain (Hughes, 2012).
Generalized-α method	A time marching method to approximate time derivatives with an arbitrary precision (Behnoudfar et al., 2020b).

Subsequently, nonlinear viscoelastic models were proposed as alternatives to the assumption of sinusoidal formations. An explanation for the localized folds studies a strut on a nonlinear elastic foundation. The results were that the buckling of the strut localizes if the foundation softens as it is deformed (Hunt et al., 1989). Such softening behavior

may originate from the nonlinear nature of the material or the multi-physics interactions (Hobbs et al., 2008). In this study, we propose a model that captures localized buckling, including the viscoelastic behavior of the foundation and the folding layer. We model the deforming layer as a plate whose lateral dimensions are much larger than its thickness. We embed this plate in a viscoelastic framework with softening-stiffening behavior. Then, following the pattern formation discussion in (Thompson and Stewart, 2002), we perform linear stability analysis to derive the dispersion relations to the thickness and mechanical properties of the plate. Next, we develop an isogeometric analysis solver with higher regularity [8, 9] to simulate the resulting system of higher-order partial differential equations and solve the resulting discrete the first-order time derivatives in time using the generalized-α method (Jansen et al., 2000). The time marching method delivers second-order accuracy as well as unconditional stability.

We organize the paper as follows. Section 2 describes the theory that supports our model and from this foundation, we derive our model in Section 3. Section 4 presents numerical results and compares the effects of viscosity. Concluding remarks are given in Section 5. Mathematical symbols are defined as they are introduced and are collated in Table 1. Table 2 provides the description of the mathematical techniques exploited in this paper.

2. Theoretical formulation

In this section, we describe our folding models for geomaterials. We consider an inextensible viscoelastic layer embedded in a viscoelastic framework. We consider a Kelvin–Voigt model in Section 2.1 and a Maxwell model in Section 2.2 to describe the viscoelastic behavior of the foundation and the plate. We model the effect of the structure's surrounding as a reaction from its foundation. For this, we utilize Winkler's idealization to represent the medium as a system of independent, closely spaced, discrete, and nonlinear elastic springs and nonlinear viscous dashpots (for more details, see (Het é nyi and Hetbenyi, 1946; Timoshenko and Woinowsky -Krieger, 1959)). Figs. 1 and 2 sketch our model in 1D and 2D.

2.1. Kelvin–Voigt viscoelastic model

We start with the Kelvin–Voigt framework to model the viscoelastic response of the medium. Since the springs and dashpots representing the elastic and viscous behaviors, respectively, are arranged in parallel, the Kelvin–Voigt model states that the strains in each component are equal:

$$\varepsilon_{total} = \varepsilon_e = \varepsilon_v, \tag{2.1}$$

where ε denotes the strain and subscripts e and v indicate the elastic and viscous parts, respectively. Accordingly, for the stress σ, we have:

$$\sigma_{total} = \sigma_e + \sigma_v, \tag{2.2}$$

which allows us to first derive the governing equations without the viscous behavior and later add it to the model. Thus, we define the domain Ω as:

$$\Omega := \left\{ (x_1, x_2, x_3) \in \mathbb{R}^3 : x_1, x_2 \in \Omega_0, x_3 \in [-h/2, h/2] \right\}, \tag{2.3}$$

with $\Omega_0 := (0, L_1) \times (0, L_2)$ being the surface in the middle of the plate and h denoting the plate thickness. Then, we consider compressive forces P_1 and P_2 along x_1 and x_2 directions, respectively, applied on Ω_0. Fig. 2 sketches our model. We include the in-plane and the transverse displacements to introduce the displacement field by considering the bending and shear components. The bending parts of the in-plane displacements are similar to those given by the classical plate theory (Love, 2013). We model the effects of shear on the in-plane displacements using higher-order shear deformation theories, which results in the parabolic variations of shear strains through the thickness and vanishing on the top and bottom surfaces of the plate (Hebali et al., 2014). Thus, we
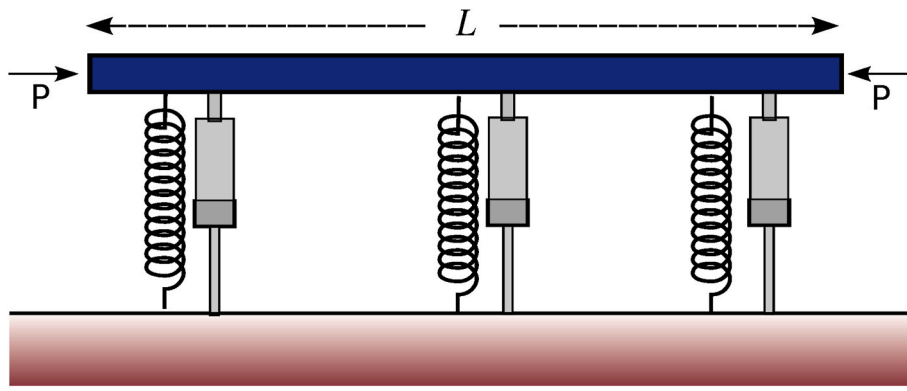
Fig. 1. Beam surrounded by viscoelastic medium (e.g., Kelvin-Voigt & Maxwell model).
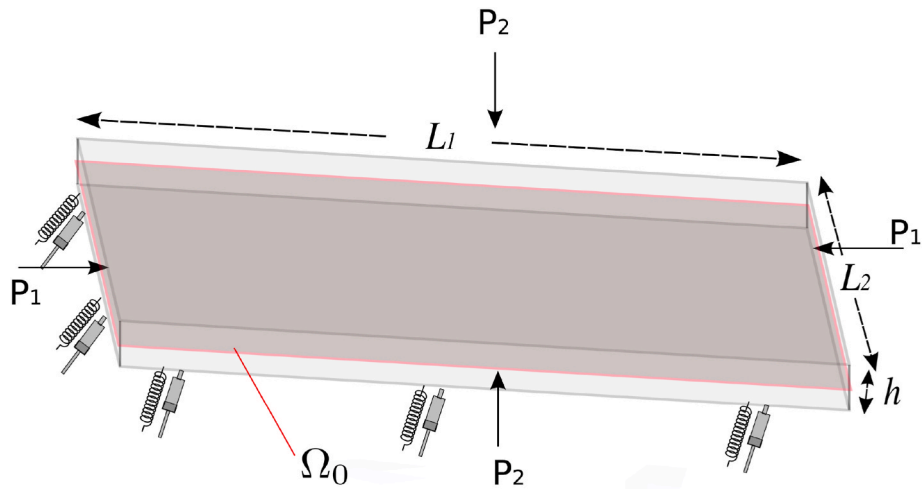
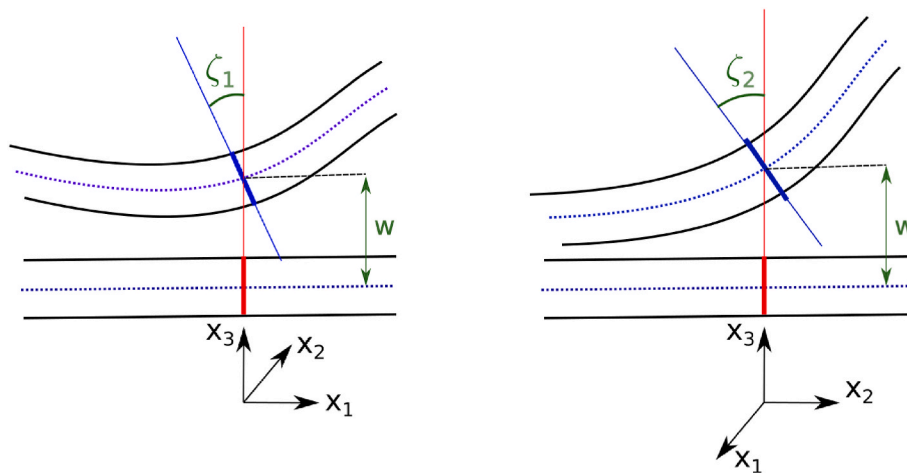**Fig. 2.** A 2D plate embedded in a viscoelastic framework.

Fig. 3. Normal vector rotation of the middle surface. The blue dotted line represents the mid-surface position. (For interpretation of the references to colour in this figure legend, the reader is referred to the Web version of this article.)

define the displacement field $\mathbf{u} = (u_1, u_2, u_3)$ as:

$$
\begin{aligned}
u_1(x_1, x_2, x_3) &= -x_3\frac{\partial w_b(x_1, x_2)}{\partial x_1} - \frac{4x_3^3}{3h^2}\frac{\partial w_s(x_1, x_2)}{\partial x_1} \\
u_2(x_1, x_2, x_3) &= -x_3\frac{\partial w_b(x_1, x_2)}{\partial x_2} - \frac{4x_3^3}{3h^2}\frac{\partial w_s(x_1, x_2)}{\partial x_2} \\
u_3(x_1, x_2, x_3) &= w_b(x_1, x_2) + w_s(x_1, x_2)
\end{aligned}
\tag{2.4}
$$

with w_b and w_s being the vertical deformations due to the bending and shear components, respectively.

Remark 1. In our model, to simulate a 3D fold, we solve for two 2D unknowns (w_b and w_s) on the middle surface to obtain the vertical deflection $w = w_b + w_s$. Next, we update the displacement field using *(2.4)* explicitly. In the numerical examples presented in Section *4*, we show the vertical deflections w for different scenarios.

Using the von–Kármán strain–displacement relations, the strain components at an arbitrary point of the plate are related to the displacement field of the middle surface (2.4), the changes in the curvatures κ_1 and κ_2, and torsion κ_{12} of the middle surface as (Cerda and Mahadevan, 2003):

$$
\varepsilon_1 = x_3\kappa_1, \qquad \varepsilon_2 = x_3\kappa_2, \qquad \gamma_{12} = x_3\kappa_{12}. \tag{2.5}
$$

Following closely the Kirchhoff-Love theory of plates, the rotation of the normal to the mid-surface reads (Love, 2013):

$$
\zeta_1 = \frac{\partial w(x_1, x_2)}{\partial x_1}, \qquad \zeta_2 = \frac{\partial w(x_1, x_2)}{\partial x_2}, \tag{2.6}
$$

where ζ_1 and ζ_2 are the rotation with respect to the directions x_1 and x_2, respectively (see, Fig. 3).

Thus, from (2.4), we define the in-plane strains as:

$$
\varepsilon_1 = -x_3\frac{\partial^2 w_b(x_1, x_2)}{\partial x_1^2} - \frac{4x_3^3}{3h^2}\frac{\partial^2 w_s(x_1, x_2)}{\partial x_1^2}, \tag{2.7}
$$

$$
\varepsilon_2 = -x_3\frac{\partial^2 w_b(x_1, x_2)}{\partial x_2^2} - \frac{4x_3^3}{3h^2}\frac{\partial^2 w_s(x_1, x_2)}{\partial x_2^2}, \tag{2.8}
$$

$$
\varepsilon_{12} = -2x_3\frac{\partial^2 w_b(x_1, x_2)}{\partial x_1 \partial x_2} - \frac{8x_3^3}{3h^2}\frac{\partial^2 w_s(x_1, x_2)}{\partial x_1 \partial x_2}. \tag{2.9}
$$

We include the transverse shear strains using the following representation:

$$
\varepsilon_{13} = \left(1 - \frac{4x_3^2}{h^2}\right)\frac{\partial w_s(x_1, x_2)}{\partial x_1}, \tag{2.10}
$$

$$
\varepsilon_{23} = \left(1 - \frac{4x_3^2}{h^2}\right)\frac{\partial w_s(x_1, x_2)}{\partial x_2}, \tag{2.11}
$$

which implies that the transverse shear strains become zero at the top ($z = h/2$) and bottom ($z = -h/2$) surfaces of the plate. Next, using the Kelvin-Voigt viscoelastic model for the plate, the constitutive law reads (Lakes and Lakes, 2009):

$$
\sigma(t) = \mathbb{E}\varepsilon(t) + \tau_c\mathbb{E}\frac{\partial\varepsilon(t)}{\partial t}, \tag{2.12}
$$

where τ_c is the viscoelastic relaxation parameter and $\mathbb{E}$ is the elastic tensor. Thus, we have:

$$
\sigma_1(t) = \frac{E}{1 - \nu^2}(\varepsilon_1 + \nu\varepsilon_2) + \tau_c\frac{E}{1 - \nu^2}\left(\frac{\partial\varepsilon_1}{\partial t} + \nu\frac{\partial\varepsilon_2}{\partial t}\right), \tag{2.13}
$$

$$
\sigma_2(t) = \frac{E}{1 - \nu^2}(\varepsilon_2 + \nu\varepsilon_1) + \tau_c\frac{E}{1 - \nu^2}\left(\frac{\partial\varepsilon_2}{\partial t} + \nu\frac{\partial\varepsilon_1}{\partial t}\right), \tag{2.14}
$$

$$
\sigma_{12}(t) = \frac{E}{2(1 + \nu)}\varepsilon_{12} + \tau_c\frac{E}{2(1 + \nu)}\frac{\partial\varepsilon_{12}}{\partial t}, \tag{2.15}
$$

$$
\sigma_{13}(t) = \frac{E}{2(1 + \nu)}\varepsilon_{13} + \tau_c\frac{E}{2(1 + \nu)}\frac{\partial\varepsilon_{13}}{\partial t}, \tag{2.16}
$$

$$
\sigma_{23}(t) = \frac{E}{2(1 + \nu)}\varepsilon_{23} + \tau_c\frac{E}{2(1 + \nu)}\frac{\partial\varepsilon_{23}}{\partial t}. \tag{2.17}
$$

We apply compressive loads P_i, $i = 1, 2$ on the plate such that the edge of the plate at the direction i is shifted horizontally by a distance δ_i which we approximate as:

$$
\begin{aligned}
\delta_1(w) &= L_1 \times h - \int_{\Omega_0}\int_{-h/2}^{h/2} 1 - \frac{1}{2}\left(\frac{\partial w}{\partial x_1}\right)^2 + \mathcal{O}\left(\left(\frac{\partial w}{\partial x_1}\right)^4\right), \\
\delta_2(w) &= L_2 \times h - \int_{\Omega_0}\int_{-h/2}^{h/2} 1 - \frac{1}{2}\left(\frac{\partial w}{\partial x_2}\right)^2 + \mathcal{O}\left(\left(\frac{\partial w}{\partial x_2}\right)^4\right).
\end{aligned}
\tag{2.18}
$$

Finally, we add the support of the framework as a resistive vertical force applied locally to the plate as:

$$
\begin{aligned}
f(w_b + w_s) &= f_e(w_b + w_s) + f_v(w_b + w_s) \\
&= k_1(w_b + w_s) - k_2(w_b + w_s)^3 + k_3(w_b + w_s)^5 + \eta(\dot{w}_b + \dot{w}_s), \quad k_i, \eta > 0,
\end{aligned}
\tag{2.19}
$$

where $f_e(u)$ and $f_v(u)$ are elastic and viscoelastic effects, respectively. $\dot{w}$ denotes the time-derivative of w. From (2.13), (2.18), and (2.19), we can derive our model as:

$$
\begin{aligned}
&D\Delta^2 w_b + 2\tau_c D\Delta^2\dot{w}_b + cF\Delta^2 w_s + 2\tau_c cF\Delta^2\dot{w}_s \\
&\quad + P_1\Delta_1 w_b + P_2\Delta_2 w_b + f(w_b + w_s) = 0. \\
&cF\Delta^2 w_b + 2\tau_c cF\Delta^2\dot{w}_b + c^2 H\Delta^2 w_s + 2\tau_c c^2 H\Delta^2\dot{w}_s - A^s\Delta w_s - 2\tau_c A^s\Delta\dot{w}_s \\
&\quad + P_1\Delta_1 w_s + P_2\Delta_2 w_s + f(w_b + w_s) = 0,
\end{aligned}
\tag{2.20}
$$

where Δ is the Laplacian operator defined as $\Delta w = \frac{\partial^2 w}{\partial x_1^2} + \frac{\partial^2 w}{\partial x_2^2}$ and $\Delta_i w = \frac{\partial^2 w}{\partial x_i^2}$. Also, we have that:

$$
\begin{aligned}
D &= \frac{Eh^3}{12(1 - \nu^2)}, & F &= \frac{Eh^5}{80(1 - \nu^2)}, \\
H &= \frac{Eh^7}{448(1 - \nu^2)}, & A^s &= \frac{4Eh}{15(1 + \nu)}.
\end{aligned}
\tag{2.21}
$$

The dimensional analysis allows us to state the dimensionless model as:

$$
\begin{aligned}
&\Delta^2 w_b + \lambda\Delta^2\dot{w}_b + \frac{1}{5}\Delta^2 w_s + \frac{1}{5}\lambda\Delta^2\dot{w}_s + P\Delta w_b + w_b + w_s - (w_b + w_s)^3 \\
&\quad + \mu(w_b + w_s)^5 + \dot{w}_b + \dot{w}_s = 0, \\
&\frac{1}{5}\Delta^2 w_b + \frac{1}{5}\lambda\Delta^2\dot{w}_b + \frac{1}{21}\Delta^2 w_s + \frac{1}{21}\lambda\Delta^2\dot{w}_b - A_D^s\Delta w_s - \lambda A_D^s\Delta\dot{w}_s + P\Delta w_s \\
&\quad + w_b + w_s - (w_b + w_s)^3 + \mu(w_b + w_s)^5 + \dot{w}_b + \dot{w}_s = 0.
\end{aligned}
\tag{2.22}
$$

where we set $P_1 = P_2$, and define the following scaling coefficients:

$$
\begin{aligned}
x_1 &\to \left(\frac{D}{k_1}\right)^{1/4} x_1, & x_2 &\to \left(\frac{D}{k_1}\right)^{1/4} x_2, & w_b &\to \sqrt{\frac{k_1}{k_2}}w_b, \\
w_s &\to \sqrt{\frac{k_1}{k_2}}w_s, & P &\to \frac{P}{\sqrt{Dk_1}}, & \mu &\to \frac{k_1 k_3}{k_2^2}, \\
A_D^s &\to \frac{A^s}{\sqrt{Dk_1}}, & t &\to \frac{\eta}{k_1}t, & \lambda &\to \frac{2\tau_c k_1}{\eta t}.
\end{aligned}
$$

According to the model (2.22), the deflection w_b and w_s depend on the parameters λ, μ, A_D^s and the applied force P. We discussed the effect of $0 < \mu \le 1$ in the response of the framework in details. Here, we pick $\mu = 0.25$ and $\mu = 0.3$. In numerical examples, we choose the viscosity of the plate $\tau_c = 0$ for an elastic fold and $\tau_c = 50\frac{\eta^2}{k_1^2}$ for viscoelastic folds
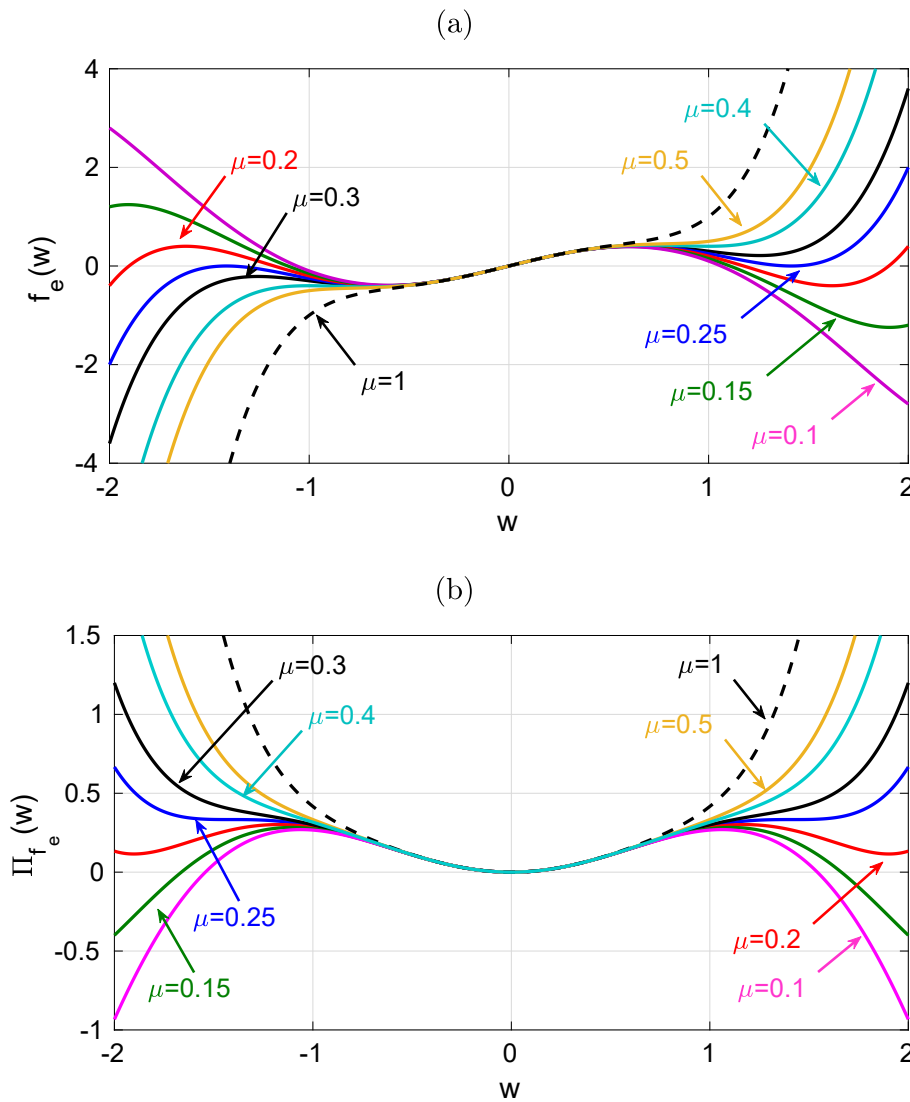
(a)

(b)

Fig. 4. The softening and re-stiffening behavior of elastic force f_e (upper pane), and the evolution of its corresponding energy functional imposed by the foundation (lower pane). Considering the elastic contribution of the embedding framework $f_e(w) = w - w^3 + \mu w^5$, we take $\mu = 0.2$ (red line). In figure (a), for small downward vertical deflections (negative w), the elastic force ($f_e(w) < 0$) favours of the deformation (softening). Further deformation gently stiffens the embedding framework as the elastic force decreases and becomes positive. The framework depicts a similar behavior for upward vertical deflections $w > 0$. That is, the elastic force is positive and afterward becomes negative. Figure (b) shows the evolution of the corresponding energy functional Π_{f_e}, showing symmetrical behavior across $w = 0$ with the functional increasing as $|w|$ tends to 1 for low μ, and decreasing as $|w|$ tends to 0 for large μ. (For interpretation of the references to colour in this figure legend, the reader is referred to the Web version of this article.)

which results in $\lambda = 100$. The layer thickness enters through (2.21).

Remark 2. We can include the overburden pressure in the model as an additional term to the forcing *(2.19)*; a constant negative term added to the model that favors downward deformations. Adding this term does not change the approach behind our analysis and numerical simulations.

2.2. Maxwell viscoelastic model

Here, we modify (2.20) to allow the folding layers to be a Maxwell material. Considering the effect of a constant strain rate in a maxwell material, the constitutive model (2.12) rewritten as (Roylance, 2001):

$$\sigma(t) = \varphi(t)\, \mathbb{E}\, \frac{\partial \varepsilon(t)}{\partial t}, \tag{2.23}$$

where $\varphi(t) = \tau_c \left(1 - e^{-\frac{t}{\tau_c}}\right)$. The derivation follows the steps of the previous section where we derive a model using the Kelvin-Voigt response. Then, following a similar logic, the conventional dimensional analysis allows us to state the dimensionless model as:

$$\widehat{\lambda}(t)\Delta^2\dot{w}_b + \frac{1}{5}\widehat{\lambda}(t)\Delta^2\dot{w}_s + P\Delta w_b + w_b + w_s - (w_b + w_s)^3$$

$$+ \mu(w_b + w_s)^5 + \dot{w}_b + \dot{w}_s = 0,$$

$$\frac{1}{5}\widehat{\lambda}(t)\Delta^2\dot{w}_b + \frac{1}{21}\widehat{\lambda}(t)\Delta^2\dot{w}_s - \widehat{\lambda}(t)A_D^s\Delta\dot{w}_s + P\Delta w_s$$

$$+ w_b + w_s - (w_b + w_s)^3 + \mu(w_b + w_s)^5 + \dot{w}_b + \dot{w}_s = 0. \tag{2.24}$$

where we set $P_1 = P_2$, and define the following scaling coefficients:

$$x_1 \rightarrow \left(\frac{D}{k_1}\right)^{1/4} x_1, \quad x_2 \rightarrow \left(\frac{D}{k_1}\right)^{1/4} x_2, \quad w_b \rightarrow \sqrt{\frac{k_1}{k_2}} w_b,$$

$$w_s \rightarrow \sqrt{\frac{k_1}{k_2}} w_s, \quad P \rightarrow \frac{P}{\sqrt{Dk_1}}, \quad \mu \rightarrow \frac{k_1 k_3}{k_2^2},$$

$$A_D^s \rightarrow \frac{A^s}{\sqrt{Dk_1}}, \quad t \rightarrow \frac{\eta}{k_1} t, \quad \widehat{\lambda}(t) \rightarrow \frac{2\varphi(t)k_1}{\eta t}.$$

Remark 3. In *(2.24)*, we can write the time-dependent parameter $\widehat{\lambda}(t)$ as:

$$\widehat{\lambda}(t) = \frac{\varphi(t)}{\tau_c}\lambda = \left(1 - e^{-\frac{t}{\tau_c}}\right)\lambda; \tag{2.25}$$

thus, after starting the simulations, $\widehat{\lambda}(t)$ approaches to λ very fast due

to the exponential in its definition. We show this evolution in Figure 7.

3. Linear-stability analysis

3.1. Kelvin-Voigt viscoelastic model

We analyse the model's behavior by rewriting (2.22) as:

$$\dot{w} := \Psi(w), \tag{3.1}$$

where $w = w_b + w_s$. We first find the fixed points of the models in (2.22). For this, we require to find the stationary point of the energy functional, which is equivalent to the zeros of the resistive force $f_e(w) = w - w^3 + \mu w^5$. Thus, we have:

$$
\begin{aligned}
w_0 &= 0, \\
w_{\pm 1} &= \pm\sqrt{\frac{1 - \sqrt{1 - 4\mu}}{2\mu}}, \\
w_{\pm 2} &= \pm\sqrt{\frac{1 + \sqrt{1 - 4\mu}}{2\mu}}.
\end{aligned}
\tag{3.2}
$$

Here, the elastic behavior couples other processes to the elastic behavior as deformation proceeds. Softening results from the opening of fractures and pores as well as from the formation of elastically soft minerals. Hardening results from the closing of fractures and pores as well as from the formation of elastically hard minerals (Hobbs et al., 2008; Hunt et al., 1989).

In our model, the elastic response of the foundation initially softens under loading; once the displacements become large enough, its response stiffens due to the cubic–quintic non-linear terms. Increasing the vertical displacement leads to softening the foundation due to the cubic term energetically favorable to buckle the beam further. As this deflection progresses, the quintic term increases, and eventually, this quintic term dominates and stiffens the foundation. We show this behavior in Fig. 4. In the upper pane of this figure, for initial deflections of the plate, the signs of f_e and w are similar. That is, f_e helps the plate to deflect more. This also increases the corresponding energy Π_{f_e} (see, the lower pane of Fig. 4). Next, for $0 < \mu \leq 0.25$, increasing the vertical deflection of the plate w, the elastic force f_e becomes zero and then increases its resistivity to the deformation. The evolution of Π_{f_e} also validates this behavior as the energy decreases and is not in favour of the deflection anymore. From (3.2), we conclude that to have softening and re-stiffening behavior in the framework, one requires to choose $0 < \mu \leq 0.25$, as Fig. 4 shows.

Then, linearizing the nonlinear model in the vicinity of the fixed points $w_\star$ using small perturbations, we obtain:

$$w(\cdot, t) = w_\star + \delta w(\cdot, t). \tag{3.3}$$

Inserting the perturbation ansatz (3.3) into (3.1), we have

$$g(w_\star + \delta w(\cdot, t)) \approx g(w_\star) + g'(w_\star)\delta w(\cdot, t) = g'(w_\star)\delta w(\cdot, t) \tag{3.4}$$

Thus, we find that a linear ODE governs the growth of the perturbation $\delta w(\cdot, t)$, that is

$$\frac{d}{dt}\delta w(\cdot, t) = g'(w_\star)\delta w(\cdot, t) \tag{3.5}$$

with the solution of

$$\delta w(\cdot, t) = \delta w(\cdot, 0)\exp(g'(w_\star)t). \tag{3.6}$$

Therefore, if $g'(w_\star) > 0$, the perturbation grows in the temporal domain, and the fixed point is linearly unstable. Whereas, for $g'(w_\star) > 0$, the fixed point shows stable behavior, and the perturbation decays with the limit value of

$$\lim_{t \to \infty}\delta w(\cdot, t) = 0. \tag{3.7}$$

For further analysis, we consider a perturbation function for w_b and w_s in the form:

$$\delta w(\cdot, t) = \varepsilon\exp(\sigma t - i\mathbf{k}\cdot\mathbf{x}), \tag{3.8}$$

where $\mathbf{x} := (x_1, x_2)$, and $\mathbf{k} := (k_{x1}, k_{x2})$ is defined as the vector of modes in x_1 and x_2 directions. That is, k_{xi} denotes the number of waves in direction x_i. Substituting (3.8) into the model (2.20), we solve the obtained relation to obtain σ. Thus, the dispersion relations for the model (2.22) around the fixed points (3.2) read:

$$
\begin{aligned}
\sigma_0(\mathbf{k}) &= \frac{-1}{1 + \lambda|\mathbf{k}|^4}\left(|\mathbf{k}|^4 - P|\mathbf{k}|^2 + 1\right), \\
\sigma_{\pm 1,}(\mathbf{k}) &= \frac{-1}{\mu\left(1 + \lambda|\mathbf{k}|^4\right)}\left(\mu\left(|\mathbf{k}|^4 - P|\mathbf{k}|^2 - 4\right) + d_{\pm 1}\right), \\
\sigma_{\pm 2}(\mathbf{k}) &= \frac{-1}{\mu\left(1 + \lambda|\mathbf{k}|^4\right)}\left(\mu\left(|\mathbf{k}|^4 - P|\mathbf{k}|^2 - 4\right) + d_{\pm 2}\right).
\end{aligned}
\tag{3.9}
$$

with $|\mathbf{k}| = \sqrt{k_x^2 + k_y^2}$ being the magnitude of the vector $\mathbf{k}$. Also, we define

$$
\begin{aligned}
d_{pm1} &= \pm(1 - \sqrt{1 - 4\mu}), \\
d_{pm2} &= \pm(1 + \sqrt{1 - 4\mu}).
\end{aligned}
\tag{3.10}
$$

The dispersion relations (3.9) shows that the model is stable when the applied force P is compressive and $\lambda \geq 0$. Around other fixed points $w_{\pm 1}$ and $w_{\pm 2}$, it is required to have $\lambda \geq 0$ and large modes.

Remark 4. Relation between the thickness and dispersion We express the dispersion relations in (3.9) as a function of the thickness of the plate and the mechanical parameters of the plate and framework. For this, we substitute the perturbation (3.8) into (2.20) to obtain:

$$
\begin{aligned}
\sigma_0(\mathbf{k}) &= \frac{-12(1 - \nu^2)}{12\eta(1 - \nu^2) + 2\tau_c Eh^3|\mathbf{k}|^4}\left(\frac{Eh^3}{12(1 - \nu^2)}|\mathbf{k}|^4 - P|\mathbf{k}|^2 + k_1\right), \\
\sigma_{\pm 1}(\mathbf{k}) &= \frac{-12(1 - \nu^2)}{k_3\left(12\eta(1 - \nu^2) + 2\tau_c Eh^3|\mathbf{k}|^4\right)} \\
&\quad \left(k_3\left(\frac{Eh^3}{12(1 - \nu^2)}|\mathbf{k}|^4 - P|\mathbf{k}|^2 - 4k_1\right) \pm \left(k_2^2 - k_2\sqrt{k_2^2 - 4k_1k_3}\right)\right), \\
\sigma_{\pm 2}(\mathbf{k}) &= \frac{-12(1 - \nu^2)}{k_3\left(12\eta(1 - \nu^2) + 2\tau_c Eh^3|\mathbf{k}|^4\right)} \\
&\quad \left(k_3\left(\frac{Eh^3}{12(1 - \nu^2)}|\mathbf{k}|^4 - P|\mathbf{k}|^2 - 4k_1\right) \pm \left(k_2^2 + k_2\sqrt{k_2^2 - 4k_1k_3}\right)\right).
\end{aligned}
\tag{3.11}
$$

3.2. Maxwell viscoelastic model

Plugging the perturbation (3.8) into model (2.24), we obtain the following time-dependent dispersion relations as:

$$
\begin{aligned}
\sigma_0(\mathbf{k}, t) &= \frac{-1}{1 + \widehat{\lambda}(t)|\mathbf{k}|^4}\left(-P|\mathbf{k}|^2 + 1\right), \\
\sigma_{\pm 1,}(\mathbf{k}, t) &= \frac{-1}{\mu\left(1 + \widehat{\lambda}(t)|\mathbf{k}|^4\right)}\left(\mu\left(-P|\mathbf{k}|^2 - 4\right) + d_{\pm 1}\right), \\
\sigma_{\pm 2}(\mathbf{k}, t) &= \frac{-1}{\mu\left(1 + \widehat{\lambda}(t)|\mathbf{k}|^4\right)}\left(\mu\left(-P|\mathbf{k}|^2 - 4\right) + + d_{\pm 2}\right).
\end{aligned}
\tag{3.12}
$$

From the dispersion relations (3.12), we conclude that the model is stable when the applied force P is compressive and $\widehat{\lambda}(t) \geq 0$. Around other fixed points $w_{\pm 1}$ and $w_{\pm 2}$, it is required to have $\widehat{\lambda}(t) \geq 0$, compressive P, and large modes such that:
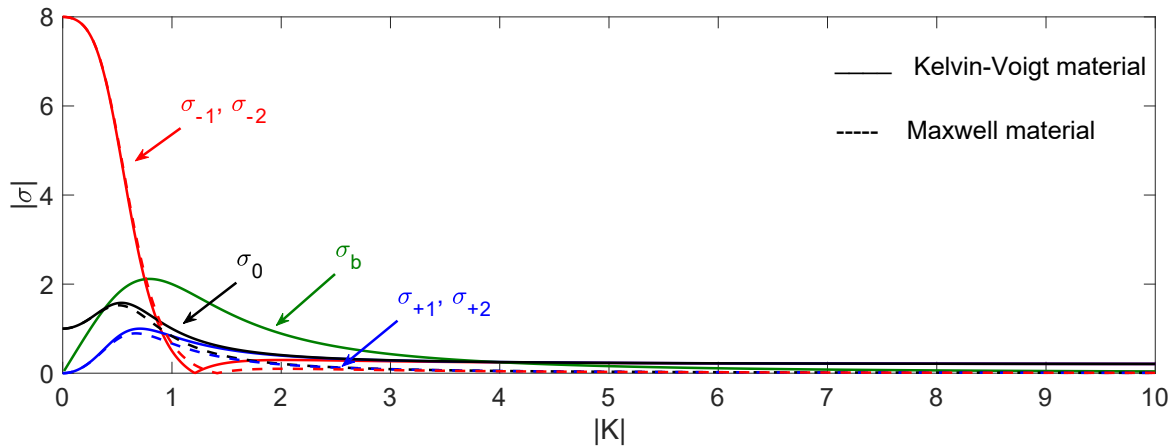
Fig. 5. Biot's relation (σ_b) predicts one wavelength for each k value. The nonlinear terms in our model capture various waves for each value of k. .
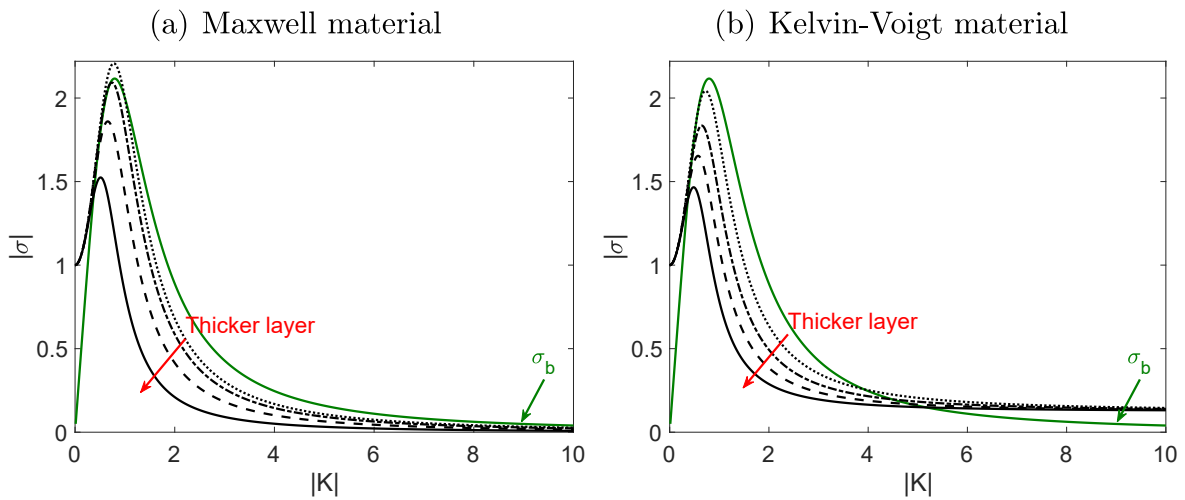

Fig. 6. The thickness effect on the dispersion relation σ_0 for the Maxwell (left) and Kelvin-Voigt materials (right).

$$P|\mathbf{k}|^2 \geq \left| -4 \pm \frac{1}{\mu}\left(1 - \sqrt{1-4\mu}\right) \right|, \qquad \text{for points } w_{\pm 1},$$

$$P|\mathbf{k}|^2 \geq \left| -4 \pm \frac{1}{\mu}\left(1 + \sqrt{1-4\mu}\right) \right|, \qquad \text{for points } w_{\pm 2}.$$

$$(3.13)$$

Remark 5. Relation between the thickness and dispersion in layer with Maxwell's behavior: We derive the dispersion relations in *(3.12)* as a function of the plate's thickness and mechanical parameters as:

$$\sigma_0(\mathbf{k},t) = \frac{-12(1-\nu^2)}{12\eta(1-\nu^2) + 2\varphi(t)Eh^3|\mathbf{k}|^4}\left(-P|\mathbf{k}|^2 + k_1\right),$$

$$\sigma_{\pm 1}(\mathbf{k},t) = \frac{-12(1-\nu^2)}{k_3\left(12\eta(1-\nu^2) + 2\varphi(t)Eh^3|\mathbf{k}|^4\right)}$$

$$\left(k_3\left(-P|\mathbf{k}|^2 - 4k_1\right) \pm \left(k_2^2 - k_2\sqrt{k_2^2 - 4k_1k_3}\right)\right), \qquad (3.14)$$

$$\sigma_{\pm 2}(\mathbf{k},t) = \frac{-12(1-\nu^2)}{k_3\left(12\eta(1-\nu^2) + 2\varphi(t)Eh^3|\mathbf{k}|^4\right)}$$

$$\left(k_3\left(-P|\mathbf{k}|^2 - 4k_1\right) \pm \left(k_2^2 + k_2\sqrt{k_2^2 - 4k_1k_3}\right)\right).$$

3.3. Dispersion relations: discussion

Next, we compare the dispersion relations of the Kelvin-Voigt and

Maxwell materials against Biot's predictions (see, e.g. (M ü hlhaus et al., 1998),). We set $\lambda = \widehat{\lambda} = 5$, $P = -4$, $\mu = 0.25$ σ_b denotes the Biot's dispersion relation. Fig. 5 shows that Biot's model does not predict the folds that appear in the nonlinear model. Besides, the Kelvin-Voigt and Maxwell materials predict similar dispersion relations. Fig. 6 shows the effect of the layer thickness on the dispersion σ_0. By decreasing the thickness, σ_0 of models (2.20) and (2.24) approaches the dispersion predicted by Biot's model σ_b.

3.4. Maximum dispersion relations

In this way, using (3.9), we obtain the maximum dispersion, $\mathbf{k}_m = |\mathbf{k}|$, in a Kelvin-Voigt material. Thus, we have:

$$\mathbf{k}_{m,0} = \sqrt{\frac{\sqrt{\lambda^2 + \lambda(P^2-2)+1}+\lambda-1}{\lambda P}} \qquad \rightarrow \max(\sigma_0)$$

$$\mathbf{k}_{m,\pm 1} = \sqrt{\frac{\frac{1}{2}\sqrt{(-2d_{\pm 1}\lambda + 8\lambda\mu + 2\mu)^2 + 4\lambda\mu^2 P^2} + d_{\pm 1}\lambda - 4\lambda\mu - \mu}{\lambda\mu P}} \qquad \rightarrow \max(\sigma_{\pm 1})$$

$$\mathbf{k}_{m,\pm 2} = \sqrt{\frac{\frac{1}{2}\sqrt{(-2d_{\pm 2}\lambda + 8\lambda\mu + 2\mu)^2 + 4\lambda\mu^2 P^2} + d_{\pm 2}\lambda - 4\lambda\mu - \mu}{\lambda\mu P}} \qquad \rightarrow \max(\sigma_{\pm 2})$$
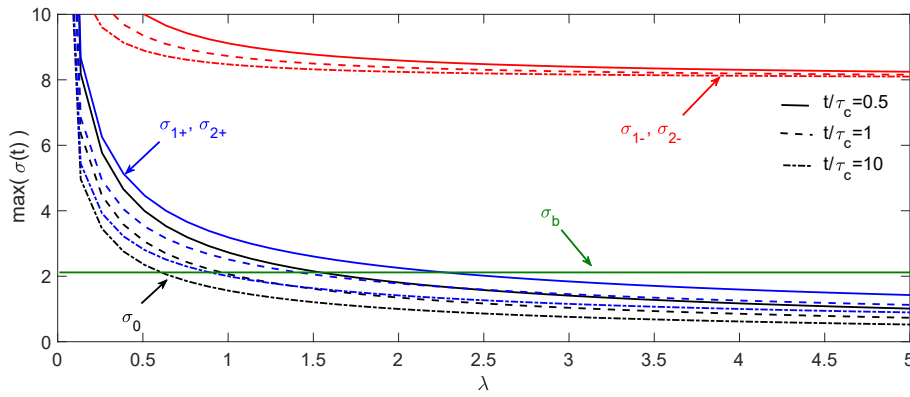
$$(3.15)$$

Fig. 7. Comparison between the Maxwell (time-dependent) maximum dispersion values and Biot's prediction. The maximum dispersions become constant when λ is large enough. The horizontal green line with constant behavior is Biot's predicted dispersion. The red, blue, and black lines show the temporal evaluation of dispersions around their corresponding points. (For interpretation of the references to colour in this figure legend, the reader is referred to the Web version of this article.)
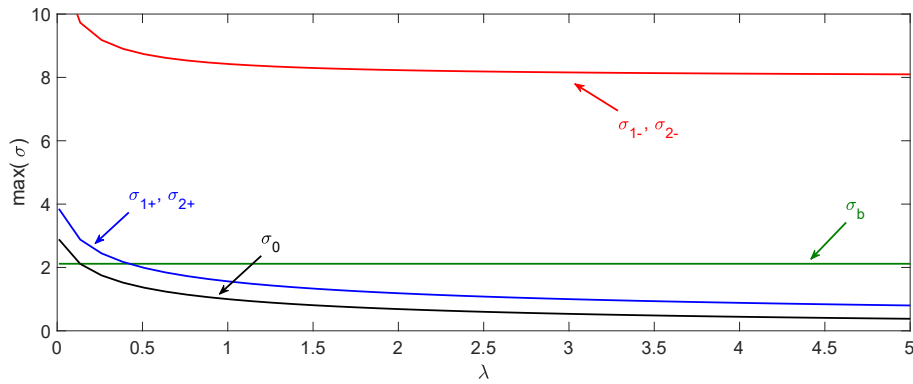

Fig. 8. Comparison between the Kelvin-Voigt (time-independent) maximum dispersion values and Biot's prediction. As before, the maximum dispersions become constant when λ is large enough.

where, from (2.20), we obtain:

$$
\max(\sigma_0) = \frac{\sqrt{\lambda(\lambda + P^2 - 2) + 1} - \lambda - 1}{2\lambda},
$$

$$
\max(\sigma_{\pm 1}) = \frac{(-d_{\pm 1}\lambda + (-1 + 4\lambda)\mu + \sqrt{(-d_{\pm 1}\lambda + \mu + 4\lambda\mu)^2 + \lambda\mu^2 P^2})}{2\lambda\mu},
$$

$$
\max(\sigma_{\pm 2}) = \frac{(-d_{\pm 2}\lambda + (-1 + 4\lambda)\mu + \sqrt{(-d_{\pm 2}\lambda + \mu + 4\lambda\mu)^2 + \lambda\mu^2 P^2})}{2\lambda\mu}.
$$

(3.16)

Similarly, the maximum dispersion, $\mathbf{k}_m = |\mathbf{k}|$, in a Maxwell material is

where, from (2.24), we obtain:

$$
\max(\sigma_0(t)) = \frac{1}{2}\left(\frac{\sqrt{\widehat{\lambda}(t)(\widehat{\lambda}(t) + P^2)}}{\widehat{\lambda}(t)} - 1\right),
$$

$$
\max(\sigma_{\pm 1}(t)) = \frac{-d_{\pm 1}\widehat{\lambda}(t) + 4\widehat{\lambda}(t)\mu + \sqrt{\widehat{\lambda}(t)(\widehat{\lambda}(t)(d_{\pm 1} - 4\mu))^2 + \mu^2 P^2)}}{2\widehat{\lambda}(t)\mu},
$$

$$
\max(\sigma_{\pm 2}(t)) = \frac{-d_{\pm 2}\widehat{\lambda}(t) + 4\widehat{\lambda}(t)\mu + \sqrt{\widehat{\lambda}(t)(\widehat{\lambda}(t)(d_{\pm 2} - 4\mu))^2 + \mu^2 P^2)}}{2\widehat{\lambda}(t)\mu}.
$$

(3.18)

$$
\mathbf{k}_{m,0}(t) = \sqrt{\frac{\sqrt{\widehat{\lambda}(t)(\widehat{\lambda}(t) + P^2)} + \widehat{\lambda}(t)}{\widehat{\lambda}(t)P}} \quad \to \max(\sigma_0(t)),
$$

$$
\mathbf{k}_{m,\pm 1}(t) = \sqrt{\frac{\sqrt{\widehat{\lambda}(t)(d_{\pm 1}^2\widehat{\lambda}(t) - 8d_{\pm 1}\widehat{\lambda}(t)\mu + \mu^2(16\widehat{\lambda}(t) + P^2))} + d_{\pm 1}\widehat{\lambda}(t) - 4\widehat{\lambda}(t)\mu}{\widehat{\lambda}(t)\mu P}}
$$
$$
\to \max(\sigma_{\pm 1}(t)),
$$

$$
\mathbf{k}_{m,\pm 2}(t) = \sqrt{\frac{\sqrt{\widehat{\lambda}(t)(d_{\pm 2}^2\widehat{\lambda}(t) - 8d_{\pm 2}\widehat{\lambda}(t)\mu + \mu^2(16\widehat{\lambda}(t) + P^2))} + d_{\pm 2}\widehat{\lambda}(t) - 4\widehat{\lambda}(t)\mu}{\widehat{\lambda}(t)\mu P}}
$$
$$
\to \max(\sigma_{\pm 2}(t)),
$$

(3.17)

(a) $\lambda = 0$, $t = 5$ (b) $\lambda = 0$, $t = 100$ (c) $\lambda = 0$, $t = 200$

(d) $\lambda = 100$, $t = 5$ (e) $\lambda = 100$, $t = 100$ (f) $\lambda = 100$, $t = 200$

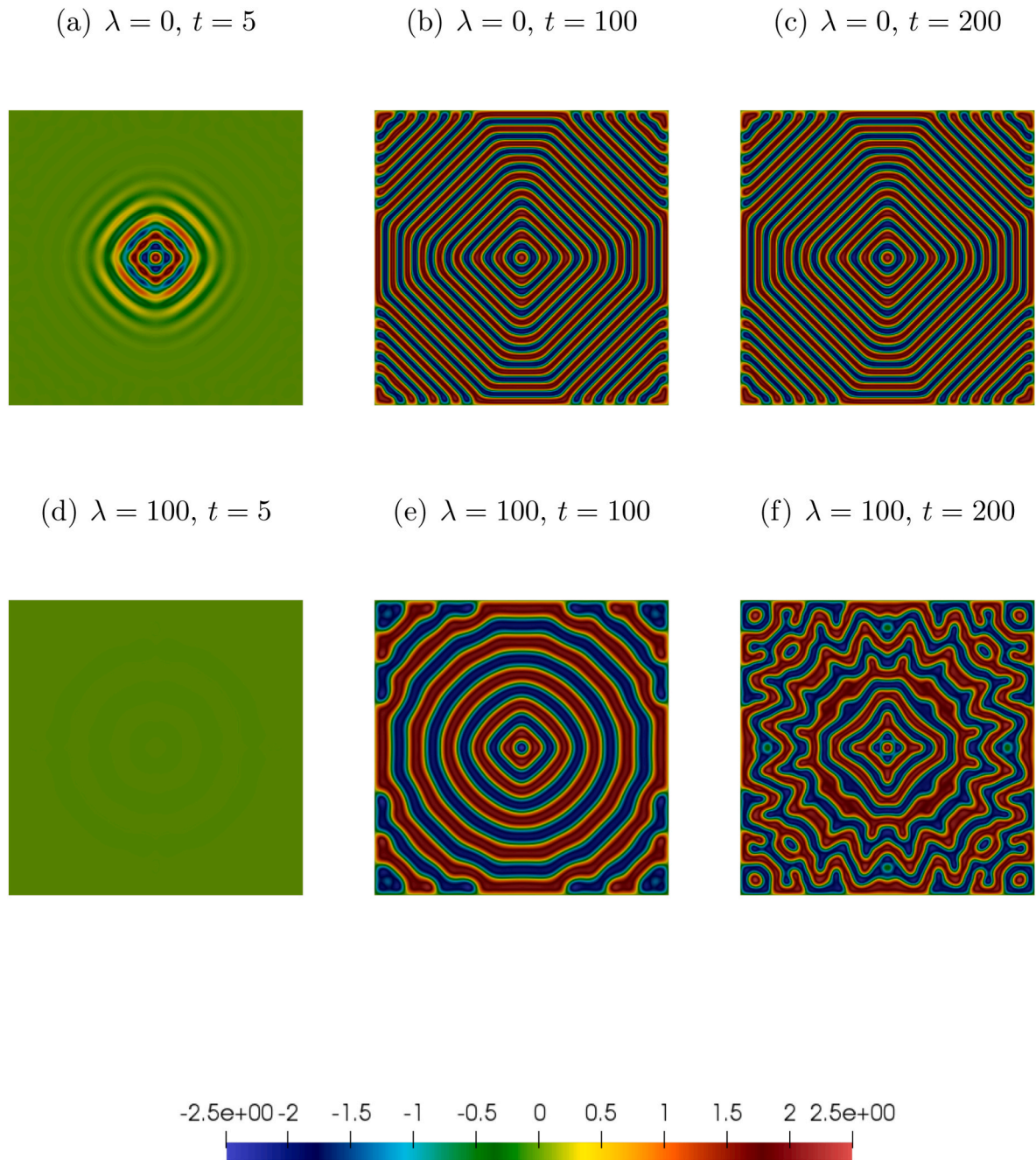-2.5e+00 -2   -1.5   -1   -0.5   0   0.5   1   1.5   2   2.5e+00

Fig. 9. The plate's mid-surface evolution Ω_0. The deformation of the elastic layer (top row) depicts a sinusoidal pattern, and the viscoelastic layer (bottom row) shows localized deformation during the folding.

Remark 6. Relation between the maximum dispersion and thickness: Here, to complete our discussion, we describe the dependency of the maximum dispersion $\mathbf{k}_m$ on the layer thickness. For this, we substitute the scaling factors of model *(2.20)* into *(3.15)* to obtain the following for the Kelvin-Voigt viscoelasticity model:

$$\mathbf{k}_{m,0} = \frac{\sqrt{\sqrt{-\frac{h^3 k_1 E}{\nu^2 - 1}}\left(\eta t\left(\sqrt{\frac{h^3 E(\eta t - 2k_1 \tau_c)^2 - 24\eta(\nu^2 - 1)P^2 \tau \tau_c}{\eta^2 h^3 t^2 E}} - 1\right) + 2k_1 \tau_c\right)}{k_1 P \tau_c}}}{2\sqrt[4]{3}}. \quad (3.19)$$

Figs. 7 and 8, show how the maximum dispersion changes relative to the non-dimensional viscosity λ for the models (2.24) and (2.20). Both figures suggest that the maximum predicted dispersion remains constant when λ becomes larger than four. Furthermore, the time-dependent dispersion relations based on the Maxwell model converge by increasing the time.

4. Numerical results

We now simulate the temporal evolution of the buckling of a $2D$ plate embedded in a viscoelastic framework. For this, firstly, we derive the weak form of the partial differential equation (2.22). Then, we use isogeometric analysis for the spatial discretization and derive the semi-discrete problem. Isogeometric analysis allows us to have sufficiently regular (for example, here, C^1) basis functions (see (Cottrell et al., 2009; Cottrell et al., 2006)).

Following standard notation for the Lebesgue and Sobolev spaces, we define a functional space $\mathcal{V} = \mathcal{H}^2$ as a Sobolev space of square-integrable
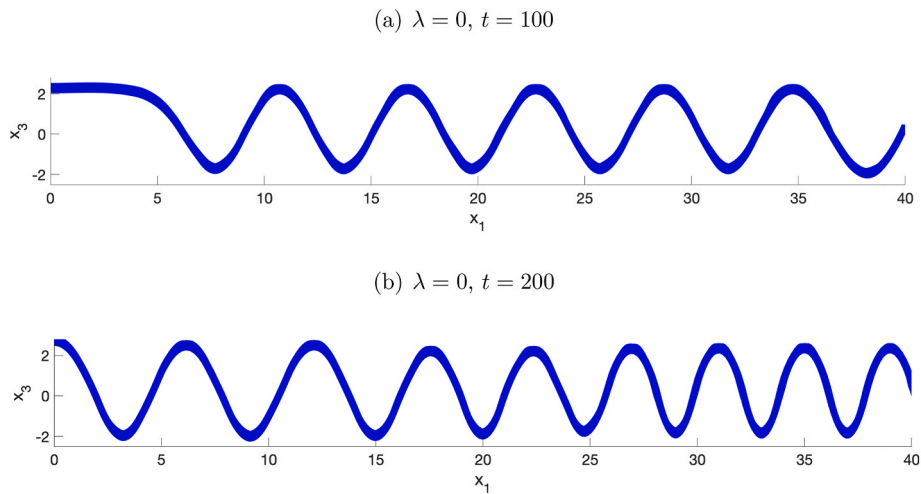
(a) $\lambda = 0$, $t = 100$

(b) $\lambda = 0$, $t = 200$

Fig. 10. The plate's cross-section evolution at $x_2 = 4$ for the case of elastic layer.

functions with square-integrable first and second derivatives. Next, we multiply (2.22) by test functions v, $r \in \mathcal{V}$. Then, using integration by parts, the variational formulation is stated as follow: Find w_b, $w_s \in \mathcal{V}$, such that:

$$B(w_b, w_s, v, r) = 0, \qquad \forall v, r \in \mathcal{V}, \tag{4.1}$$

where

$B(w_b, w_s, v, r):$

$$
= \begin{cases}
(\Delta w_b, \Delta v) + (\lambda \Delta \dot{w}_b, \Delta v) + \frac{1}{5}(\Delta w_s, \Delta v) + \frac{1}{5}(\lambda \Delta \dot{w}_s, \Delta v) \\
-(P \nabla w_b, \nabla v) + (w_b + w_s - (w_b + w_s)^3 + \mu(w_b + w_s)^5, v) \\
+(\dot{w}_b + \dot{w}_s, v) = 0, \\
\frac{1}{5}(\Delta w_b, \Delta r) + \frac{1}{5}(\lambda \Delta \dot{w}_b, \Delta r) + \frac{1}{21}(\Delta w_s, \Delta r) + \frac{1}{21}(\lambda \Delta \dot{w}_s, \Delta r) \\
-(A_D^s \nabla w_s, \nabla r) - (\lambda A_D^s \nabla \dot{w}_s, \nabla r) - (P \nabla w_s, \nabla r) \\
+(\dot{w}_b + \dot{w}_s + w_b + w_s - (w_b + w_s)^3 + \mu(w_b + w_s)^5, r) = 0,
\end{cases}
$$

$$\tag{4.2}$$

Then, we use an isogeometric analysis (IGA) discretization and

define $\mathcal{P}_h$ as a partition of the spatial domain Ω into elements K and obtain $\Omega_h := \bigcup_{K \in \mathcal{P}_h} K$. This allows us to discrete (4.1) in space, and use the Galerkin method to approximate (4.1) by the following variational problems over the finite-dimensional spaces: find $w_b^h, w_s^h \in \mathcal{V}^h \subset \mathcal{V}$ such that:

$$B(w_b^h, w_s^h, v^h, r^h) = \mathbf{0}, \qquad \forall v^h, r^h \in \mathcal{V}^h, \tag{4.3}$$

with trial solutions w_b^h, w_s^h, defined as:

$$w_b^h = \sum_{A=1}^{n_b} w_{bA} N_A, \qquad w_s^h = \sum_{A=1}^{n_b} w_{sA} N_A, \tag{4.4}$$

and the weighting functions v^h, r^h as:

$$v^h = \sum_{A=1}^{n_b} v_A N_A, \qquad r^h = \sum_{A=1}^{n_b} r_A N_A. \tag{4.5}$$

Here, N_A is the basis function, and n_b is the dimension of the discrete space. Based on the definition of $\mathcal{V}_h$, we need the discrete space to be at least $\mathcal{H}^2$-conforming globally. In this work, we satisfy this requirement by using a non-uniform rational B-spline (NURBS) basis with C^1-continuity.

We derive the fully-discrete problem by partitioning the time interval $[0, T]$ with a time step τ and use the generalized-α method (Behnoudfar et al., 2020a, 2021; Jansen et al., 2000). Finally, we denote by W_b^n, W_s^n the approximations to $w_b^h(t_n), w_s^h(t_n)$, respectively.
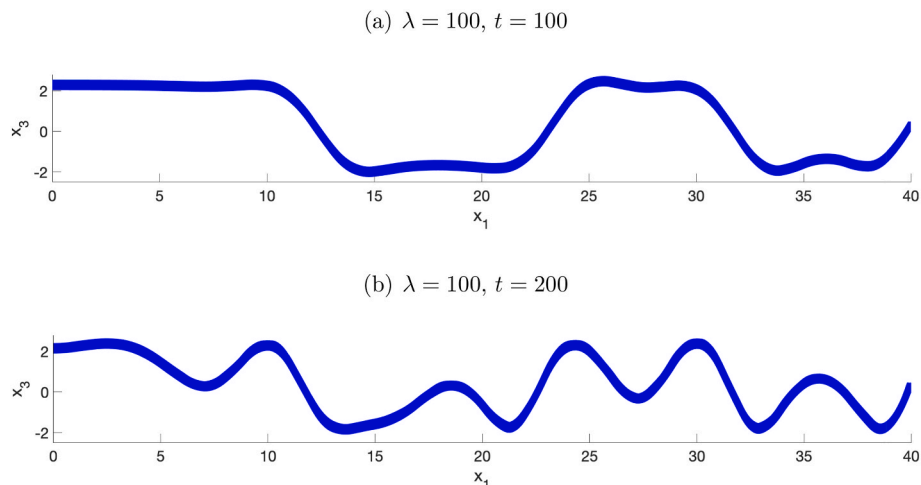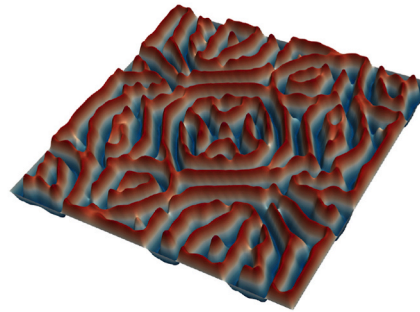
Remark 7.

(a) $\lambda = 100$, $t = 100$
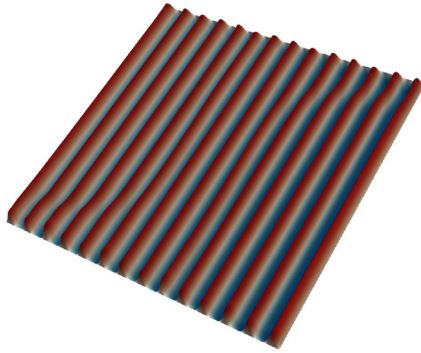
(b) $\lambda = 100$, $t = 200$

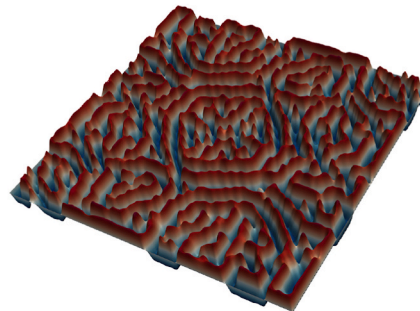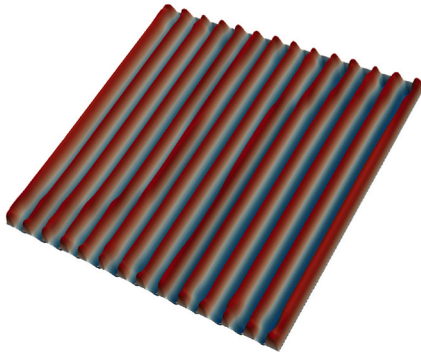**Fig. 11.** The plate's cross-section evolution at $x_2 = 4$.

(a) $P_1 = 40, P_2 = 20, t = 5$

(b) $P_1 = P_2 = 40, t = 5$

(c) $P_1 = 40, P_2 = 20, t = 10$

(d) $P_1 = P_2 = 40, t = 10$

(e) $P_1 = 40, P_2 = 20, t = 15$
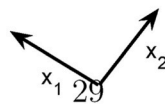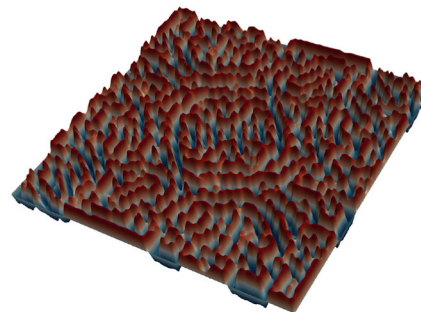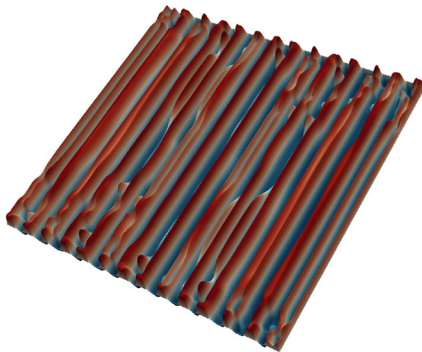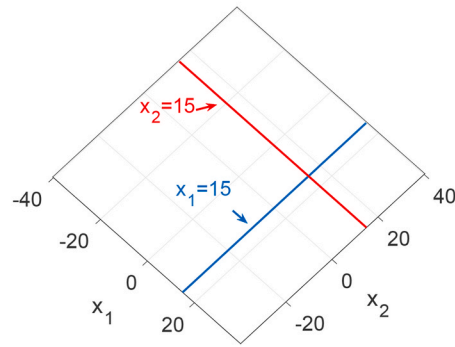
(f) $P_1 = P_2 = 40, t = 15$

x_1 x_2

Fig. 12. Mid-surface deformation of the viscoelastic layer embedded in a viscoelastic framework. Applied horizontal forces P_1, P_2 are not equal; the folds have a sinusoidal behavior at the early stages; later, the deformations localize. This localized behavior is true for all stages when $P_1 = P_2$.

(a) The position of the cross-sections

(b) Cross-section at $x_2 = 15$, $t = 5$
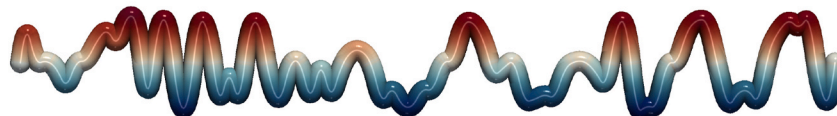

(c) Cross-section at $x_1 = 15$, $t = 5$

(d) Cross-section at $x_2 = 15$, $t = 10$

(e) Cross-section at $x_1 = 15$, $t = 10$

(f) Cross-section at $x_2 = 15$, $t = 15$
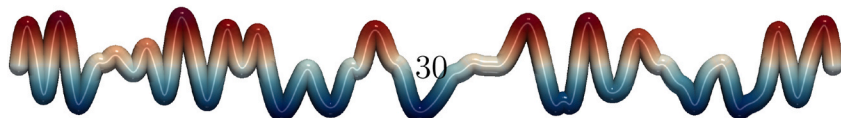

(g) Cross-section at $x_1 = 15$, $t = 15$

Fig. 13. The localized behavior of the folded layer's cross-section for the case $P_1 = P_2 = 40$. The cross-sections are plotted along the x_2 dimension at point $x_1 = 15$ and along the x_1 dimension at point $x_2 = 15$.
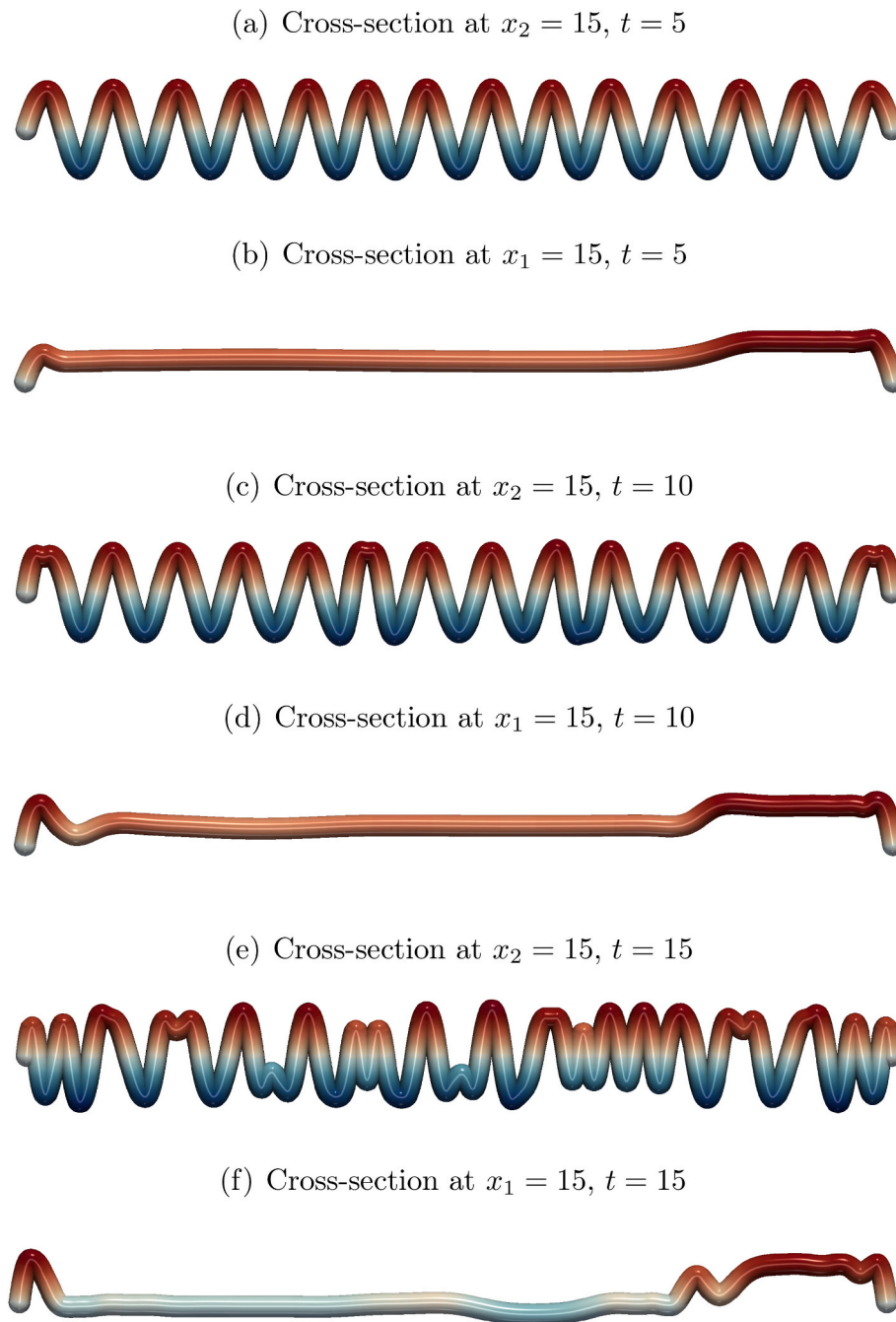
(a) Cross-section at $x_2 = 15$, $t = 5$

(b) Cross-section at $x_1 = 15$, $t = 5$

(c) Cross-section at $x_2 = 15$, $t = 10$

(d) Cross-section at $x_1 = 15$, $t = 10$

(e) Cross-section at $x_2 = 15$, $t = 15$

(f) Cross-section at $x_1 = 15$, $t = 15$

Fig. 14. Folded layer's cross-section evolution for the case $P_1 = 40$, $P_2 = 20$.

To complete our methodology for implementing the fully discrete problem, we use Newton's method to solve the resulting nonlinear equation. The iterative procedure can be summarized as computing the residual $\boldsymbol{R}^{(i)}$, using $W_{n+1}^{(i)}$ with i denoting the i-th iteration. Next, computing the Jacobian $\boldsymbol{J}^{(i)}$, we solve

$$\boldsymbol{J}^{(i)} \delta W^{(i+1)} = \boldsymbol{R}^i. \tag{4.6}$$

Then, we update $W_{n+1}^{(i+1)} = W_{n+1}^{(i)} - \delta W^{(i+1)}$. We repeat these steps until the norm of the global residual vector is below a tolerance (e.g., here, 10^{-8}) of their initial value. We usually achieve convergence in 3–5 nonlinear iterations per time step. For more details, we refer the reader to (Gómez et al., 2008; Vignal et al., 2015). The following results show the vertical deflections w on the domain. The horizontal deformations are updated based on the displacement field *(2.4)*.

We consider a 2D domain $[-40, 40] \times [-40, 40]$ and set $\mu = 0.3$ with a compressive force $P = 4$. We also use quadratic elements with C^1 continuity and time step $\tau = 0.1$. The Dirichlet conditions impose the deflection w and the curvature $\frac{\partial^2 w}{\partial x_i^2}$ on the boundaries (here, they are equal to zero). The initial condition is set to

$$w_b = \frac{0.0001}{(1+x^2)(1+y^2)}, \qquad w_s = 0. \tag{4.7}$$

We also study the effects of viscosity on the layer's displacement response and its localized buckling by comparing two cases of $\lambda = 0$ (elastic layer) and $\lambda = 100$ (viscoelastic layer). Fig. 9 presents the results. In Figs. 10 and 11 we show the cross-sections of the plate with thickness of $h = 0.5$ for elastic and viscoelastic plates, respectively. The viscous contribution in the layer delays the deformation. Compared with
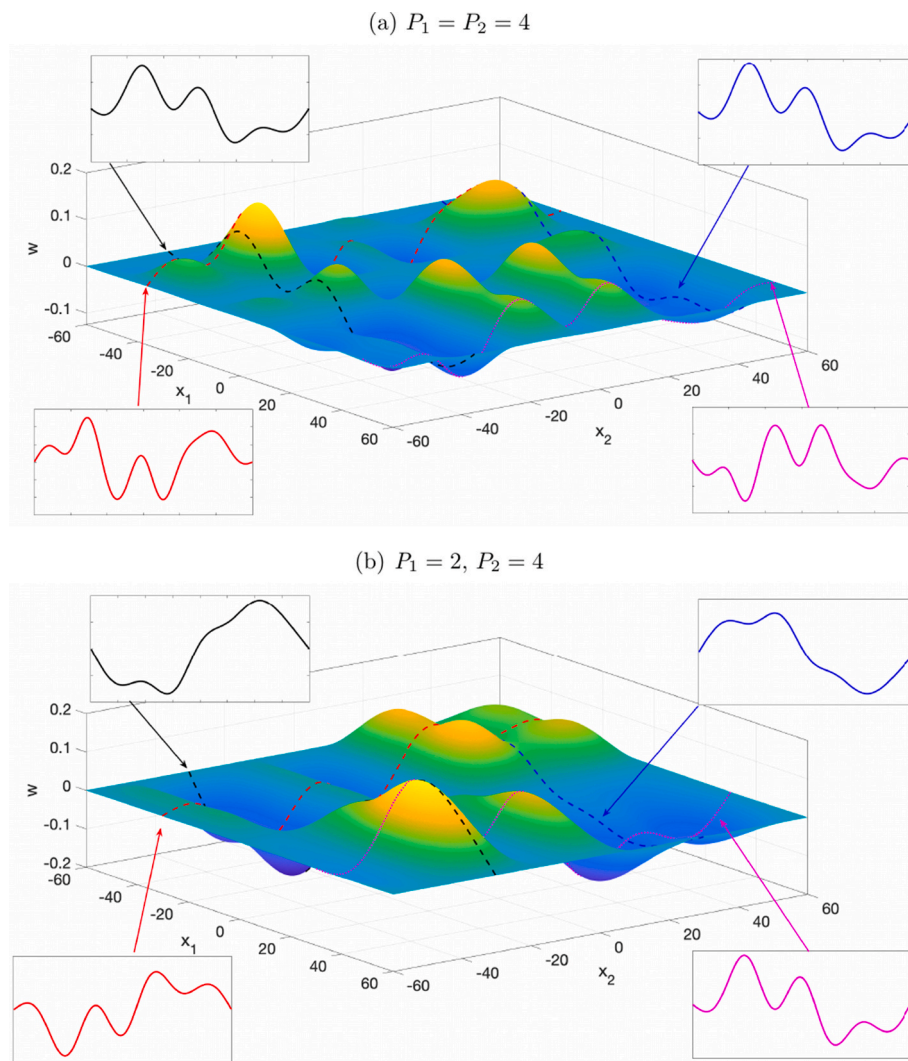
(a) $P_1 = P_2 = 4$

(b) $P_1 = 2, P_2 = 4$

Fig. 15. Folded layer's cross-section evolution. In (a), $P_1 = P_2 = 4$ and the structure resembles domes and basins. In (b), $P_1 = 2, P_2 = 4$ and the structure resembles ridges and valleys.

a folded elastic layer, the evolution shows a localized behavior.

Next, we show the effect of the applied lateral forces. For this, we consider a viscoelastic layer and use our model (2.19) with $\lambda = 100$ and $\mu = 0.2$ with similar domain, boundary and initial conditions. Fig. 12 shows the evolution of folding when $P_1 = P_2$ and $P_1 = 2P_2$. We also show the evolution of the cross-section of the simulated folds for both cases of equal and non-equal lateral forces in Figs. 13 and 14, respectively. Lastly, we consider a larger domain $[-60, 60] \times [-60, 60]$. We apply compressive forces of $P_1 = P_2 = 4$, and $P_1 = 2P_2 = 4$ with $\lambda = 1$. Fig. 15 shows how the localized behavior still can be observed in both examples, showing domes and basins in (a) and more linear ridges and valleys in (b).

5. Conclusions

We derive a model that captures localized buckling, including the viscoelastic behavior of the foundation and the folding layer. Using plate theory with nonlinear softening-stiffening behavior, we embed a plate in a viscoelastic framework. Then, we use the high-order shear deformation theory to incorporate shear strains in the thick layer parallel to the layering during folding. This shearing adds a nonlinearity that results in localized folding. We perform a linear stability analysis to derive the dispersion relations to the thickness and mechanical properties of the plate. We use an isogeometric solver with high regularity to simulate the

resulting system of high-order partial differential equations (e.g., our model has fourth-order spatial derivatives) and solve the resulting semi-discrete problem using the generalized-α method. This time marching method delivers second-order accuracy as well as unconditional stability. We show in the numerical examples how the viscoelastic layers deflect locally. Also, we provide numerical evidence on how the horizontal applied forces impact the folding. The horizontal loading helps us describe how dome and basin and linear ridges and valleys form according to the relative magnitudes of the applied forces.

The physical model we introduce also shows the following:

- Increasing the layer thickness increases the importance of layer parallel shearing, which results in localized folding for situations where the Biot analysis predicts strictly periodic folding.
- The dispersion relationships are a function of strain (time), whereas Biot's dispersion relation is time independent.
- For thick layers, more than one wavelength may amplify, as Fig. 5 shows, as opposed to Biot's result where only one wavelength amplifies.
- The relation between layer thickness and amplification is highly nonlinear, as Section 3.2 indicates. The wavelength increases as the layer thickness grows, as Fig. 6 shows, and is always larger than Biot's wavelength, as Fig. 5 indicates.

- The buckling behavior of both Kelvin-Voigt and Maxwell materials is similar. Hence, from a geological point of view, their response may not be discernible from the available data.
- Lastly, we introduce a relation to describe the maximum dispersion as a function of layer thickness as

$$\lim_{h^3 \to 0} k_m = \frac{\sqrt{\frac{\eta k_2^2 t \sqrt{\frac{k_1 E}{1-\nu^2}}\sqrt{\frac{96 k_1^2 k3^2 (1-\nu^2) P^2 \tau_c}{\eta k_2^4 t E}}}{2\left(k_1^2 k3 P \tau_c\right)}}}{2 \times 3^{1/4}} \qquad (5.1)$$

Declaration of competing interest

The authors declare the following financial interests/personal relationships which may be considered as potential competing interests: Victor Calo reports financial support was provided by European Union's Horizon 2020 research. Victor Calo reports financial support was provided by Curtin Corrosion Centre.

References

Atkinson, K.E., 2008. An Introduction to Numerical Analysis. John wiley & sons.

Behnoudfar, P., Calo, V.M., Deng, Q., Minev, P.D., 2020a. A variationally separable splitting for the generalized-α method for parabolic equations. Int. J. Numer. Methods Eng. 121 (5), 828–841.

Behnoudfar, P., Deng, Q., Calo, V.M., 2020b. High-order generalized-alpha method. Appl. Eng. Sci. 4, 100021.

Behnoudfar, P., Deng, Q., Calo, V.M., 2021. Higher-order Generalized-α Methods for Parabolic Problems arXiv preprint arXiv:2102.05910.

Blay, P., Cosgrove, J., Summers, J., 1977. An experimental investigation of the development of structures in multilayers under the influence of gravity. J. Geol. Soc. 133 (4), 329–342.

Cerda, E., Mahadevan, L., 2003. Geometry and physics of wrinkling. Phys. Rev. Lett. 90 (7), 074302.

Cobbold, P., 1976. A discussion on natural strain and geological structure-fold shapes as functions of progressive strain. Phil. Trans. Roy. Soc. Lond. Math. Phys. Sci. 283 (1312), 129–138.

Cottrell, J.A., Hughes, T.J.R., Bazilevs, Y., 2009. Isogeometric Analysis: toward Integration of CAD and FEA. John Wiley & Sons.

Cottrell, J.A., Reali, A., Bazilevs, Y., Hughes, T.J.R., 2006. Isogeometric analysis of structural vibrations. Comput. Methods Appl. Mech. Eng. 195 (41), 5257–5296.

Fletcher, R.C., 1974. Wavelength selection in the folding of a single layer with power-law rheology. Am. J. Sci. 274 (9), 1029–1043.

Gómez, H., Calo, V.M., Bazilevs, Y., Hughes, T.J.R., 2008. Isogeometric analysis of the Cahn–Hilliard phase-field model. Comput. Methods Appl. Mech. Eng. 197 (49–50), 4333–4352.

Hebali, H., Tounsi, A., Houari, M.S.A., Bessaim, A., Bedia, E.A.A., 2014. New quasi-3d hyperbolic shear deformation theory for the static and free vibration analysis of functionally graded plates. J. Eng. Mech. 140 (2), 374–383.

Hetényi, M., Hetbenyi, M.I., 1946. Beams on Elastic Foundation: Theory with Applications in the Fields of Civil and Mechanical Engineering, vol. 16. University of Michigan press, Ann Arbor, MI.

Hobbs, B., Regenauer-Lieb, K., Ord, A., 2008. Folding with thermal–mechanical feedback. J. Struct. Geol. 30 (12), 1572–1592.

Hudleston, P., 1973. An analysis of "single-layer" folds developed experimentally in viscous media. Tectonophysics 16 (3–4), 189–214.

Hughes, T.J., 2012. The Finite Element Method: Linear Static and Dynamic Finite Element Analysis. Courier Corporation.

Hunt, G.W., Bolt, H., Thompson, J.M.T., 1989. Structural localization phenomena and the dynamical phase-space analogy. Proc. Roy. Soc. Lond. A 425 (1869), 245–267.

Jansen, K.E., Whiting, C.H., Hulbert, G.M., 2000. A generalized-α method for integrating the filtered Navier–Stokes equations with a stabilized finite element method. Comput. Methods Appl. Mech. Eng. 190 (3–4), 305–319.

Joets, A., Ribotta, R., 1988. Localized, time-dependent state in the convection of a nematic liquid crystal. Phys. Rev. Lett. 60 (21), 2164.

Kolodner, P., 1993. Coexisting traveling waves and steady rolls in binary-fluid convection. Phys. Rev. 48 (2), R665.

Lakes, R., Lakes, R.S., 2009. Viscoelastic Materials. Cambridge university press.

Lee, K.-J., McCormick, W.D., Pearson, J.E., Swinney, H.L., 1994. Experimental observation of self-replicating spots in a reaction–diffusion system. Nature 369 (6477), 215.

Love, A.E., 2013. A Treatise on the Mathematical Theory of Elasticity. Cambridge university press.

Mühlhaus, H.-B., Sakaguchi, H., Hobbs, B., 1998. Evolution of three–dimensional folds for a non–Newtonian plate in a viscous medium. Proc. Royal Soc. London. Ser A.: Math. Phys. Eng. Sci. 454 (1980), 3121–3143.

Piegl, L., Tiller, W., 1987. Curve and surface constructions using rational b-splines. Comput. Aided Des. 19 (9), 485–498.

Pirkl, S., Ribiere, P., Oswald, P., 1993. Forming process and stability of bubble domains in dielectrically positive cholesteric liquid crystals. Liq. Cryst. 13 (3), 413–425.

Ramsay, J.G., 1967. Folding and Fracturing of Rocks. Mc Graw Hill Book Company 568.

Roylance, D., 2001. Engineering Viscoelasticity, vol. 2139. Department of Materials Science and Engineering–Massachusetts Institute of Technology, Cambridge MA, pp. 1–37.

Schmalholz, S.M., Podladchikov, Y.Y., 2000. Finite amplitude folding: transition from exponential to layer length controlled growth. Earth Planet Sci. Lett. 179 (2), 363–377.

Smith, R., 1975. Unified theory of the onset of folding, boudinage, and mullion structure. Geol. Soc. Am. Bull. 86 (11), 1601–1609.

Smith, R.B., 1977. Formation of folds, boudinage, and mullions in non-Newtonian materials. Geol. Soc. Am. Bull. 88 (2), 312–320.

Thompson, J.M.T., Stewart, H.B., 2002. Nonlinear Dynamics and Chaos. John Wiley & Sons.

Timoshenko, S.P., Woinowsky-Krieger, S., 1959. Theory of Plates and Shells. McGraw-hill.

Vignal, P., Dalcin, L., Brown, D.L., Collier, N., Calo, V.M., 2015. An energy-stable convex splitting for the phase-field crystal equation. Comput. Struct. 158, 355–368.

Watkinson, A., 1976. Fold propagation and interference in a single multilayer unit. Tectonophysics 34 (3–4), T37–T42.